MDPI

Article

Pollution from Highways Detection Using Winter UAV Data

Gabriel A. Baah [1], Igor Yu. Savin [1,2,*] and Yuri I. Vernyuk [2,*]

[1] Institute of Environmental Engineering, Peoples' Friendship University of Russia (RUDN University), 6 Miklukho-Maklaya Street, 117198 Moscow, Russia

[2] V.V. Dokuchaev Soil Science Institute, Pyzhevsky St., 7, 119017 Moscow, Russia

* Correspondence: savin_iyu@esoil.ru (I.Y.S.); vernyuk_yui@esoil.ru (Y.I.V.)

Abstract: This study identified and evaluated the association between metal content and UAV data to monitor pollution from roadways. A total of 18 mixed snow samples were collected at the end of winter, utilizing a 1 m long and 10 cm wide snow collection tube, from either side of the Caspian Highway (Moscow-Tambo-Astrakhan) in Moscow. Inductively coupled plasma optical emission spectrometry (ICP-OES) was used to examine the chemical composition of the samples, yielding 35 chemical elements (metals). UAV data and laboratory findings were calculated and examined. Regression estimates demonstrated the possibility of using remote sensing data to identify Al, Ba, Fe, K, and Na metals in snow cover near roadways due to dust dispersal. This discovery supports the argument that UAV sensing data can be utilized to monitor air pollution from roadways.

Keywords: pearson correlation analysis; independent variable; metal; concentration; street dust; pollution; unmanned aerial vehicle

1. Introduction

Dust contains a variety of chemical compositions because it originates from a variety of sources, including the climate, human activities, soil particles and rocks, pollen, hair, clothing fibers, bacteria, dust mites, bits of dead bugs, microscopic specks of plastic, plant materials, and dander (dead skin cells shed by animals) [1–3]. According to ref. [4–6], road and air dust is a complex particle mixture that has the potential to transport high concentrations of different contaminants, such as metals, hydrocarbons, nutrients, particulates, de-icing salts, and mold spores, which may result in a major source of atmospheric air pollution through resuspension by wind and vehicular movements. According to ref. [7], the chemical composition and particle size of dust are crucial when assessing the consequences, and they vary across distance and time. Ref. [8] found that meteorological circumstances, the soil environment, bedrock, and human activities all substantially impacted the diversity of street dust composition. According to ref. [9], road dust is a complex combination of particles and pollutants originating from a wide range of urban, automotive, and industrial sources and activities, and its components and quality are indications of environmental pollution in big cities. Metals from atmospheric deposition can accumulate in dust by sedimentation, impaction, and interception [10]. Furthermore, metal concentrations in crops are determined by the metal content of soil and crop absorption capabilities [11], which are also directly related to soil properties such as soil organic matter [12], pH, salinity [13], and heavy metal morphology [14].

Levels of elements, particularly toxic elements, linked with non-physiologically regulated anthropogenic activities may vary depending on geographic and geochemical settings and land-use activities. The elemental composition of hair samples may reflect this, indicating environmental pollution or hot zones [15]. Metal contamination in the soil might pose an ecological problem. Cd and Hg were discovered to pose the greatest potential ecological concerns [16,17]. Metal-polluted food causes substantial health concerns to local populations, including Itai-itai disease [18] and even cancer [19]. As a result, [20], a

research study demonstrated the mutuality of the close relationship between the metal contents of dust deposits and topsoils. Ref. [21], for example, analyzed possible ecological and human health risks posed by heavy metals in soil rather than in crops, let alone their link. Exposure to these metals may have several health repercussions for this or future generations. Acute or chronic exposure to these metals has been linked to the genesis of many illnesses. Lead, for example, has been linked to anxiety, arthritis (rheumatoid and osteoporosis), attention deficit disorder, blindness, cardiovascular disease, cartilage destruction, constipation, depression, epilepsy, gout, immune repression, infertility, kidney disorder, liver dysfunction, menstrual problems, muscle weakness, spinal cord pathology, peripheral neuropathies, psychomotor dysfunction, sudden infant death syndrome, and many other conditions [22,23]. Furthermore, metals in soil can endanger human health in three ways: inhalation, dermal absorption, and soil ingestion [24]. In most circumstances, children are more vulnerable to metal contamination than adults [25]. As a result, several researchers have focused their efforts on the human health risks posed by metals in soil [26]. Previous research employed remote sensing to monitor and map marine pollution as well as investigate the relationships between metals, soils, and crops, with a particular emphasis on metal distribution and bioaccumulation. Ref. [27] utilized the combination of satellite data and UAV technology to explore the continuity of climatic and human changes in the Alps and, more extensively, on animals, biodiversity, and ecosystems in mountain and wilderness settings. The emphasis of the study was to support decision-makers involved in wildlife and domestic animal management and planning (both hunting and pastoral) as well as public health (from the perspective of One Health). Ref. [28] employed remote sensing to map oil pollution, suspended solid contents, algae blooms, and floating plastic debris in marine waterways via absorption. Ref. [29] demonstrated that data on meteorological conditions, including light pollution, can be acquired across a long vertical range (up to tens of kilometers); however, the placement of the vertical profiles was reliant on the air circumstances (mainly winds). Despite this accomplishment, tower measurements are confined to a single location and height or different heights of the same tower. Ref. [30] reported the use of remote sensing to model the relationship between predictor variables during the cross-validation process for both non-imaging and imaging sensors for clay, sand, and SOM, which are crucial in tropical soil management. Ref. [31] demonstrated the use of remote sensing for quantitative (spectral-based) soil property assessments. Unfortunately, only a few studies have employed remote sensing or UAV data to investigate the dust contamination of roadside snow. It is thus worthwhile to investigate the relationship between dust, its metal content, and snow and collect remote sensing and UAV data to monitor snow pollution.

2. Materials and Methods

Gritchino in Moscow Oblast, Russia, was chosen as the test site because of several variables, including the composition of traffic flow along the Caspian Highway (Moscow-Tambov-Astrakhan), which runs through large agricultural areas used for wheat and maize cultivation. Vehicular movement on the route had increased to over thirty thousand vehicles by 2020 [32], with traffic intensity on the route increasing more than five times since its completion in 1983. The site is located at $(54°, 36°, 15°)$ North and $(38°, 6°, 20°)$ East. It has a mild continental climate with warm summers and cold winters dominated by western or southwestern winds [33]. The major wind direction for the winter of 2021/2022 was southwest, according to the Kashira meteorological station records. The average temperature in February was $-10\ °C$. The road is flanked on both sides by fertile land [33].

Snow samples were collected at a distance of 30–190 m from both sides of the Caspian Highway (Moscow–Tambo–Astrakhan) at the end of winter 2021–2022, according to the snow sampling procedure (stratified sampling procedure) described by ref. [34]. The locations of the sampling stations were calculated using UAV parameters obtained throughout the sampling campaign, with an error of less than 10 cm. A total of 18 mixed samples (three samples were mixed at each test point) were collected using a snow collecting tube 1 m in

length and 10 cm in diameter, as illustrated in Figure 1. Each sample's snow depth was measured. The samples were subsequently taken to Moscow's V.V. Dokuchaev Soil Science Institute for processing and chemical analysis. Once 90% of the sample had melted, it was de-iced at room temperature and chilled to finish the melting process. The samples were subsequently filtered using polycarbonate filters with a pore size of 0.45 μm and diameter of 47 mm to separate the water and particles for analysis using inductively coupled plasma optical emission spectrometry (Agilent 5800 ICP-OES). Dust particles were digested into solution using nitric acid before being injected into the plasma. This was performed to bring the entire dissolved solid concentration into the instrument's operating range, thus lowering the detection limit of the technique. To allow any reaction gases to escape, the samples were allowed to stand for 10 min after 2 mL of strong nitric acid reagent was applied to each sample [35].

Figure 1. The location of the study area (54°36′15″ North, 38°6′20″ East) and collected samples in sealed buckets.

The samples were then treated with 6 mL of concentrated hydrochloric acid (SG 1.18) for another 10 min. To prevent the production of insoluble chloride salts, nitric acid was added first, followed by hydrochloric and hydrofluoric acids. The samples were subsequently heated in line with EPA Procedure 3051 in a Milestone Ethos microwave system. The samples were then heated to 175 °C for 10 min, kept between 170 and 180 °C for another 10 min following the microwave digestion procedure, and cooled for 5 min. The sample containers were transferred to a fume closet to achieve room temperature. To obtain a homogenous sample, the volume of the digest was increased with distilled water and then forcefully shaken in a 100 mL volumetric flask. The samples were allowed to settle overnight to remove any suspended solids [35]. A total of 35 chemical elements (metals) were identified. The findings of each sample were recalculated per m^2 of dust particles, per m^2 of melted water (without dust), and per snow mantle on m^2 of soil surface.

UAV images were captured concurrently with the snow sample program using a DJI Matrice 200 quadcopter. A Zenmuse X4S FC6510 20 MP camera placed on a gyrostabilized suspension was used for visible spectral range (RGB) photography.

The DJI Go4 app was used to calibrate the UAV, while the Drone Deploy app was used for general flight tasks and camera setup on the Zenmuse X4S FC6510 (see Appendix A). The drone was flown at an altitude of 60 m with an average speed of 12 m/s. The flight plan was manually predefined, with a distance of approximately 30 m between neighboring passes (conventional serpentine flight patterns) and the nadir (0°, or perpendicular to the ground) camera view angles for generating point clouds. The image overlay between passes was set to 30%.

The Drone Deploy app automatically generated a flight path and capture mode based on the model of the quadcopter and camera, the specified flight altitude, and image overlap. The shots were taken from a height of 74 m.

The airborne survey yielded georeferenced photos in JPEG and TIFF formats.

The collected aerial pictures were analyzed using Agisoft Metashape Professional, a photogrammetric program. The software can handle images in visible (RGB), infrared, and monochrome spectral regions. The parameters supplied in each photograph's metadata were utilized for this purpose.

Individual photographs with similar overlaps were stitched together using Agisoft Metashape. We obtained textured 3D terrain models in PDF, georeferenced in WGS 84 (EPSG: 4326), textured orthophotos, and digital terrain and relief models in various formats (JPEG, TIFF, KML, KMZ) from the aerial survey data processed by Agisoft Metashape. The obtained aerial survey materials and their processing were of high resolution. The resolution of the Zenmuse X4S FC6510 was 1.99 cm/pix, while the digital terrain model was 7.83 cm/pox.

Each pixel in the generated UAV photographs had a 24-bit color domain with three values: red, green, and blue (ranging from 0 to 255). The color separation for each pixel was achieved using the ILWIS v.3.3 standard option. The image's red, green, and blue values were immediately extracted. One of the following formulas was used to retrieve more color images as shown in Table 1:

Table 1. UAV color images.

Yellow	=	$255 - \text{Blue}$
Magenta	=	$255 - \text{green}$
Cyan	=	$255 - \text{red}$
Hue	=	$\text{Red} - ((\text{Green} + \text{Blue})/2) * 240/255$
Saturation	=	$\sqrt{(\text{Red}^2 + \text{Green}^2 + \text{Blue}^2 - \text{Red} * \text{Green} - \text{Red} * \text{Blue} - \text{Green} * \text{Blue})} * 240/255$
Intensity	=	$1/3 * (\text{Red} + \text{Green} + \text{Blue}) * 240/255$
Gray	=	$0.3 * \text{Red} + 0.59 * \text{Green} + 0.11 * \text{Blue}$

Red, green, and blue values ranged from 0 to 255, while hue, saturation, and intensity values ranged from 0 to 240, which complied with the Windows color scheme definition. In the formulas for hue, saturation, and intensity above, multiplication factor 240/255 was used to obtain that range.

Stata Standard Edition software for Windows 64-bit x86-64 was utilized. Correlation and regression analyses were performed to determine the nature of the relationship and the significance level between the metal content of the snow and the UAV-derived indicators (values of different colored images). Split validation and methodological concepts were used to forecast the fitness of the model used in the study (Licensed Microsoft Excel, Professional Plus 2019). Variables were split 60/40 for hypothetical testing. The predictions and coefficients of the models were similar to the technique utilized, demonstrating the validity of the approach and findings [36,37]. The sequence of the study is depicted in Figure 2.
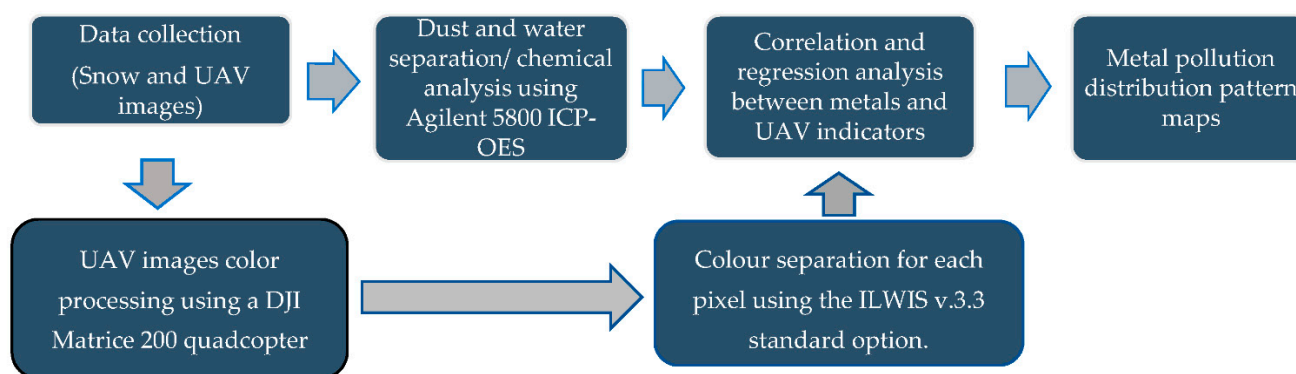
Figure 2. Workflow of metal pollution detection based on UAV data.

3. Results

3.1. Metal Content in Water

Tables A1–A4 present data on the concentrations of metals in water, dust particles, and snow as well as the acquired UAV parameters, respectively. According to these findings, the concentrations of metals such as B, Cd, Ce, Co, Cr, Gd, and Ho in water were extremely low. The most abundant elements included Al, Ca, Fe, K, Mg, Na, and Zn. The levels of visible metals in water at the sampling location nearest to the road were distinguished by their greater amounts. As a result of the visual examination, the distribution of several components in water varied with the distance from the road.

There was a strong positive correlation between metal content and the UAV parameters (blue_av, gray, green, intensity, and red) in water. Meanwhile, the hue parameter had a weak relationship with metal content. Specifically, the strong positive relationship implied that the metals were extensively diffused in water. Overall, the predominant metal in water was Na, followed by K, Fe, and Al. On the contrary, the metal content exhibited a negative correlation with the cyan, magenta, saturation, and yellow parameters in water, with correlation coefficients of 0.38 (Al), 0.30 (Fe), 0.39 (K), and 0.46 (Na). The correlation coefficients for UAV parameters are shown in Table 2.

Table 2. Correlation matrix between (Al, Fe, K, and Na) metals and UAV parameters.

Metal	Blue_av	Cyan	Gray	Green	Hue	Intensity	Magenta	Red	Saturation	Yellow
Al/m^2	0.83	−0.83	0.82	0.83	0.38	0.82	−0.83	0.83	−0.13	−0.83
Fe/m^2	0.84	−0.83	0.83	0.84	0.30	0.84	−0.84	0.83	−0.02	−0.84
K/m^2	0.62	−0.62	0.62	0.61	0.39	0.64	−0.61	0.62	−0.03	−0.62
Na/m^2	0.85	−0.85	0.85	0.84	0.46	0.86	−0.85	0.85	−0.15	−0.85

At a level of significance, Al and Fe metals demonstrated a linear regression association with the red parameter. On the other hand, K and Na had the best regression relationships with the intensity parameter. Overall, the synergistic and antagonistic impacts of the associated factors on metals in water were mostly focused on Al and Fe metals with red and K and Na metals with intensity. The red parameter, in particular, had a synergistic influence on the absorption of Al and Fe metals, whereas the intensity parameter exhibited antagonistic effects on the absorption of K and Na metals. Furthermore, levels of Al and Fe were significantly higher on the east side of the road than on the west side, compared to K and Na levels. This showed their extensive geological history. The elevated quantities of metals in water at the road's edges might well be attributed to runoff water from de-icing treatments and asphalt pavement agents. Figure 3 displays the visual distribution of metals in water according to their associated characteristics. The regression coefficients for parameters are shown in Table 3.
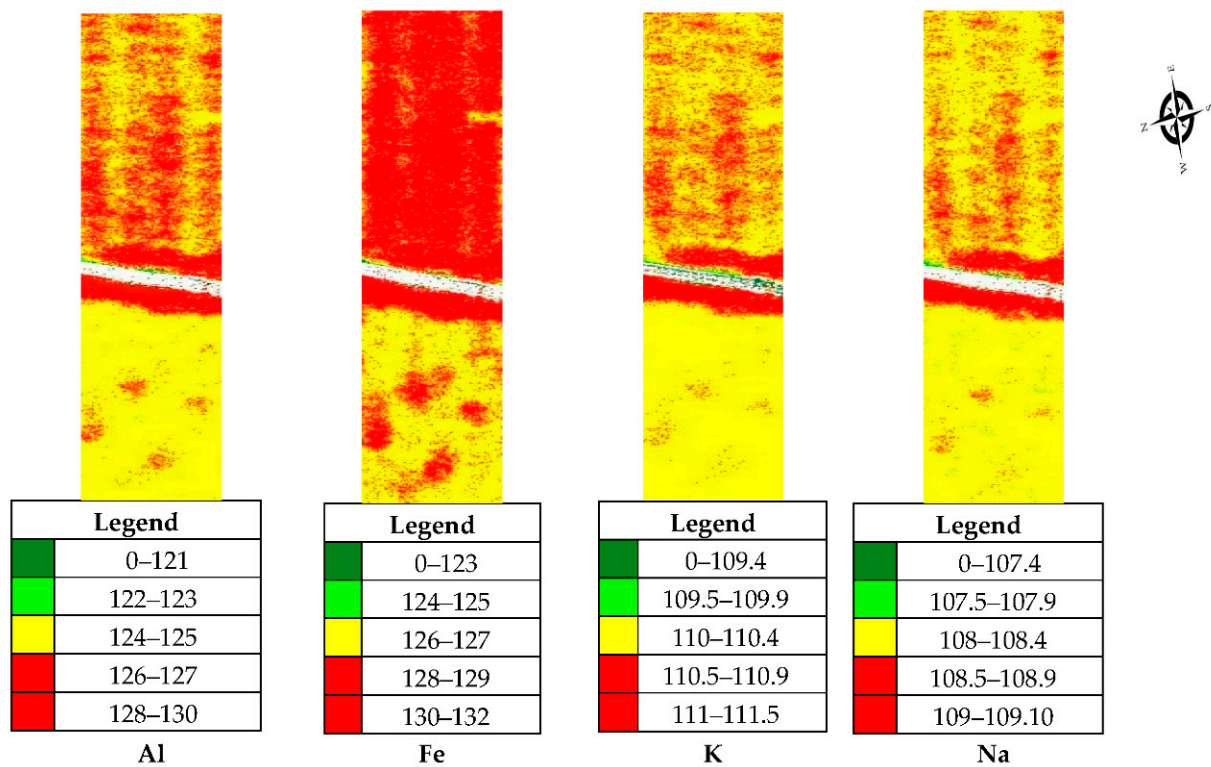
Figure 3. Distribution map of levels of (Al, Fe, K, and Na) metals in water.

Table 3. Regression estimates of (Al, Fe, K, and Na) metals and UAV parameters.

Metal	Parameter	Coefficients	*p*-Value	Formula
Al/m^2	Red	140.688 **	0.047	0.0567x + 117.67
Fe/m^2	Red	161.131 **	0.016	0.0647x + 117.05
K/m^2	Intensity	539.604 ***	0.006	0.0171x + 107.99
Na/m^2	Intensity	744.159 *	0.069	0.0083x + 107.11
Multiple R	0.936			
R Square	0.876			

***, **, and * indicate 1%, 5%, and 10% levels of significance, respectively.

3.2. Metal Content in Dust

1. The most abundant metals were Al, Ca, Fe, K, Mg, Na, and Pr. The increased levels of metals in dust at the nearest sampling stations were a distinguishing feature. Using remote sensing to detect metals in fresh snow was unlikely to be successful unless in a heavily contaminated region. Based on the relationships, several metals, such as Al, Ca, Ce, Co, Cr, Cu, Dy, Er, Fe, K, La, Li, Mg, Mn, Nd, Ni, P, Pr, Sc, Sm, Y, and Zn, highlighted the importance of dust in monitoring roadside pollution.

2. There was a significant relationship between metal content (Al, Ca, Ce, Cr, Cu, Dy, Er, Fe, K, La, Li, Mg, Mn, Nd, Ni, P, Pr, Sc, Sm, Y, and Zn) and the UAV parameters (blue av, gray, green, intensity, and red). Meanwhile, a weak correlation was observed with the hue parameter. The high positive association was an indicator of metal diffusion in dust. On the other hand, Al, Ca, Ce, Cr, Cu, Dy, Er, Fe, K, La, Li, Mg, Mn, Nd, Ni, P, Pr, Sc, Sm, Y, and Zn metals in dust exhibited a negative association with the magenta, cyan, saturation, and yellow parameters. Table 4 depicts the correlation coefficients for the metal content of dust with the UAV parameters.

Table 4. Correlation matrix between (Al, Ca, Ce, Co, Cr, Cu, Dy, Er, Fe, K, La, Li, Mg, Mn, Nd, Ni, P, Pr, Sc, Sm, Y, and Zn) metals and UAV parameters.

Metal	Blue_av	Cyan	Gray	Green	Hue	Intensity	Magenta	Red	Saturation	Yellow
Al/m^2	0.86	−0.86	0.85	0.85	0.45	0.86	−0.85	0.86	−0.10	−0.86
Ca/m^2	0.87	−0.86	0.86	0.86	0.39	0.87	−0.86	0.86	−0.05	−0.87
Ce/m^2	0.86	−0.86	0.85	0.85	0.45	0.86	−0.85	0.86	−0.09	−0.86
Co/m^2	0.88	−0.89	0.88	0.87	0.46	0.88	−0.87	0.89	−0.14	−0.88
Cr/m^2	0.91	−0.91	0.91	0.90	0.46	0.91	−0.90	0.92	−0.12	−0.91
Cu/m^2	0.87	−0.87	0.86	0.86	0.45	0.87	−0.86	0.87	−0.10	−0.87
Dy/m^2	0.81	−0.79	0.79	0.80	0.33	0.80	−0.80	0.79	0.00	−0.81
Er/m^2	0.78	−0.79	0.77	0.76	0.54	0.78	−0.76	0.79	−0.08	−0.78
Fe/m^2	0.87	−0.87	0.86	0.86	0.45	0.87	−0.86	0.87	−0.10	−0.87
K/m^2	0.88	−0.87	0.87	0.87	0.44	0.87	−0.87	0.88	−0.09	−0.88
La/m^2	0.87	−0.80	0.86	0.86	0.45	0.87	−0.86	0.87	−0.10	−0.87
Li/m^2	0.82	−0.84	0.81	0.81	0.46	0.82	−0.81	0.83	−0.12	−0.82
Mg/m^2	0.86	−0.85	0.85	0.85	0.42	0.85	−0.85	0.85	−0.07	−0.86
Mn/m^2	0.86	−0.86	0.85	0.85	0.44	0.86	−0.85	0.86	−0.09	−0.86
Nd/m^2	0.87	−0.87	0.86	0.86	0.43	0.87	−0.86	0.87	−0.08	−0.87
Ni/m^2	0.90	−0.90	0.89	0.89	0.43	0.90	−0.89	0.90	−0.08	−0.90
P/m^2	0.89	−0.89	0.88	0.88	0.41	0.89	−0.89	0.89	−0.08	−0.89
Pr/m^2	0.82	−0.83	0.82	0.81	0.52	0.82	−0.81	0.83	−0.12	−0.82
Sc/m^2	0.82	−0.83	0.82	0.81	0.52	0.83	−0.81	0.83	−0.12	−0.82
Sm/m^2	0.82	−0.83	0.82	0.81	0.52	0.83	−0.81	0.83	−0.12	−0.82
Y/m^2	0.86	−0.87	0.86	0.85	0.47	0.86	−0.85	0.87	−0.14	−0.86
Zn/m^2	0.89	−0.89	0.88	0.88	0.43	0.89	−0.88	0.89	−0.09	−0.89

Metals Al, Ca, Ce, Cr, Cu, Dy, Er, Fe, K, La, Li, Mg, Mn, Nd, Ni, P, Pr, Sc, Sm, Y, and Zn revealed a significant linear regression relationship with the red parameter. Overall, the synergistic effects of the UAV parameters on metals in dust were mostly concentrated on Al, Ca, Fe, K, and Na. Furthermore, the red parameter had a synergistic effect on the absorption of all metals along the road's edge. This was evidenced by the higher levels of Al, Ca, Fe, K, and Na metals predominantly on the east side of the road compared to the other metals in dust. The increased levels of metals at the road edges might be due to the resuspension of asphalt pavement chemicals and runoff water from de-icing treatments. Figure 4 displays the visual distribution of metals in dust according to their associated characteristics. The regression coefficients for parameters are shown in Table 5.

3.3. Metal Content in Snow (Water and Dust)

Compared to prior approaches, data from remote sensing has proven to be a superior tool for monitoring pollution along roadways in a cost-effective and ecologically acceptable manner. Furthermore, according to ref. [38], the most efficient detection of contaminants in snow is sensor-based monitoring with spatial information (GIS). This discovery verified the ability of remote sensing to identify elemental metals such as Al, Ba, Fe, K, and Na in snow.

The concentrations of metals (Al, Ba, Fe, K, and Na) and UAV parameters (blue av, gray, green, intensity, and red) in snow had a substantial positive association. However, the hue parameter had a weak relationship with metal content. The substantial positive association suggested that the metals were widely distributed in snow. Overall, Na was the most abundant metal in snow, followed by K, Fe, Al, and Ba. On the other contrary, the metal content exhibited a negative association with the cyan, magenta, saturation, and yellow parameters in snow. The correlation coefficients for the UAV parameters are shown in Table 6.

Legend		Legend		Legend		Legend		Legend	
	0–140		0–126		0–39,000		0–4000		0–9000
	150–159		127–128		40,000–49,000		5000–9000		10,000–14,000
	160–169		129–130		50,000–59,000		10,000–14,000		15,000–19,000
	170–179		131–132		60,000–69,000		15,000–19,000		20,000–24,000
	180–190		133–134		70,000–80,000		20,000–25,000		25,000–30,000
Al		**Ca**		**Ce**		**Co**		**Cr**	

Legend		Legend		Legend		Legend		Legend	
	0–3000		0–40,000		0–40,000		0–129		0–140
	4000–5000		50,000–90,000		50,000–90,000		130–134		150–190
	6000–7000		100,000–140,000		100,000–140,000		135–139		200–240
	8000–9000		150,000–190,000		150,000–190,000		140–144		250–290
	10,000–12,000		200,000–250,000		200,000–250,000		145–150		300–350

Figure 4. *Cont.*

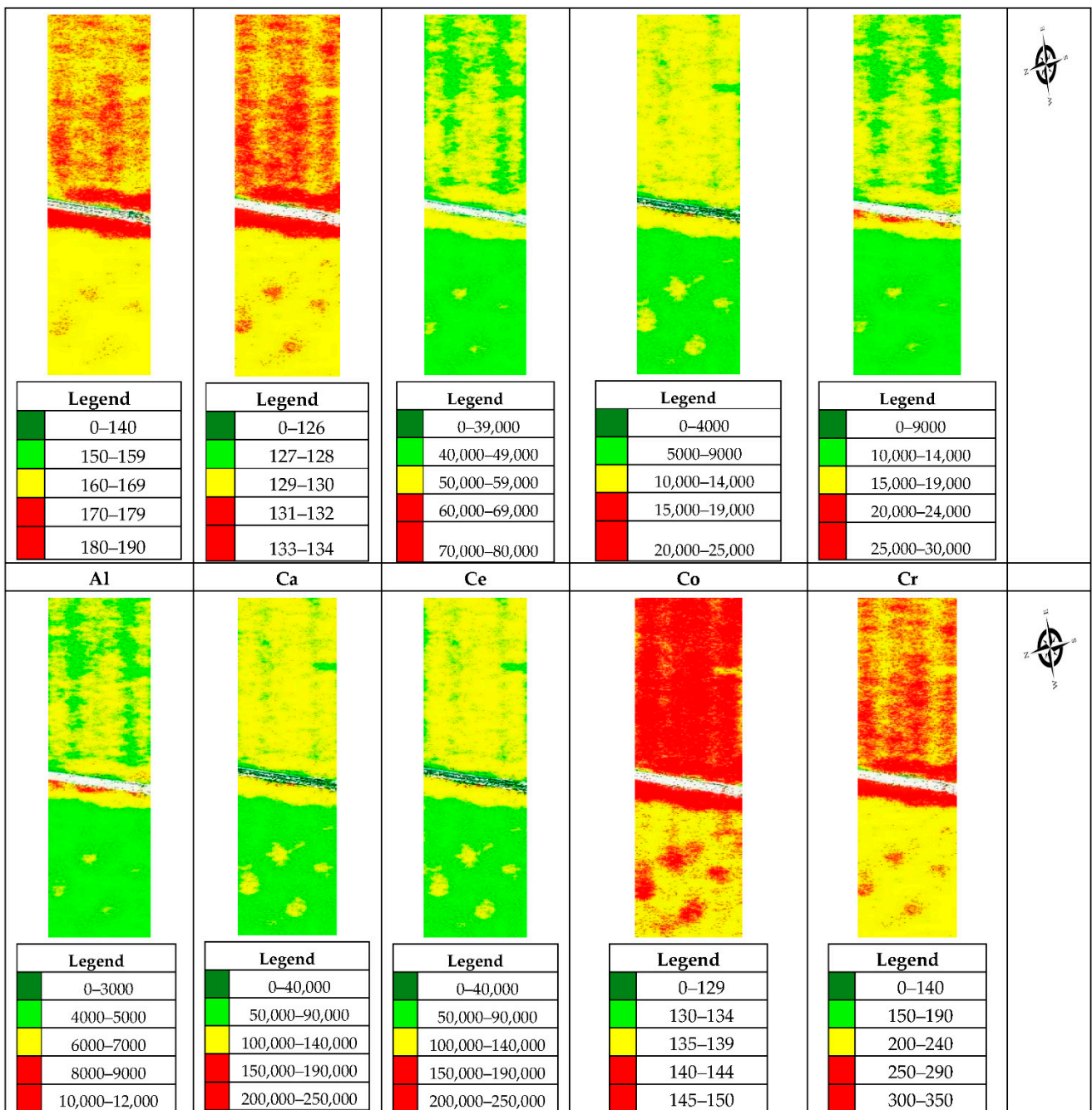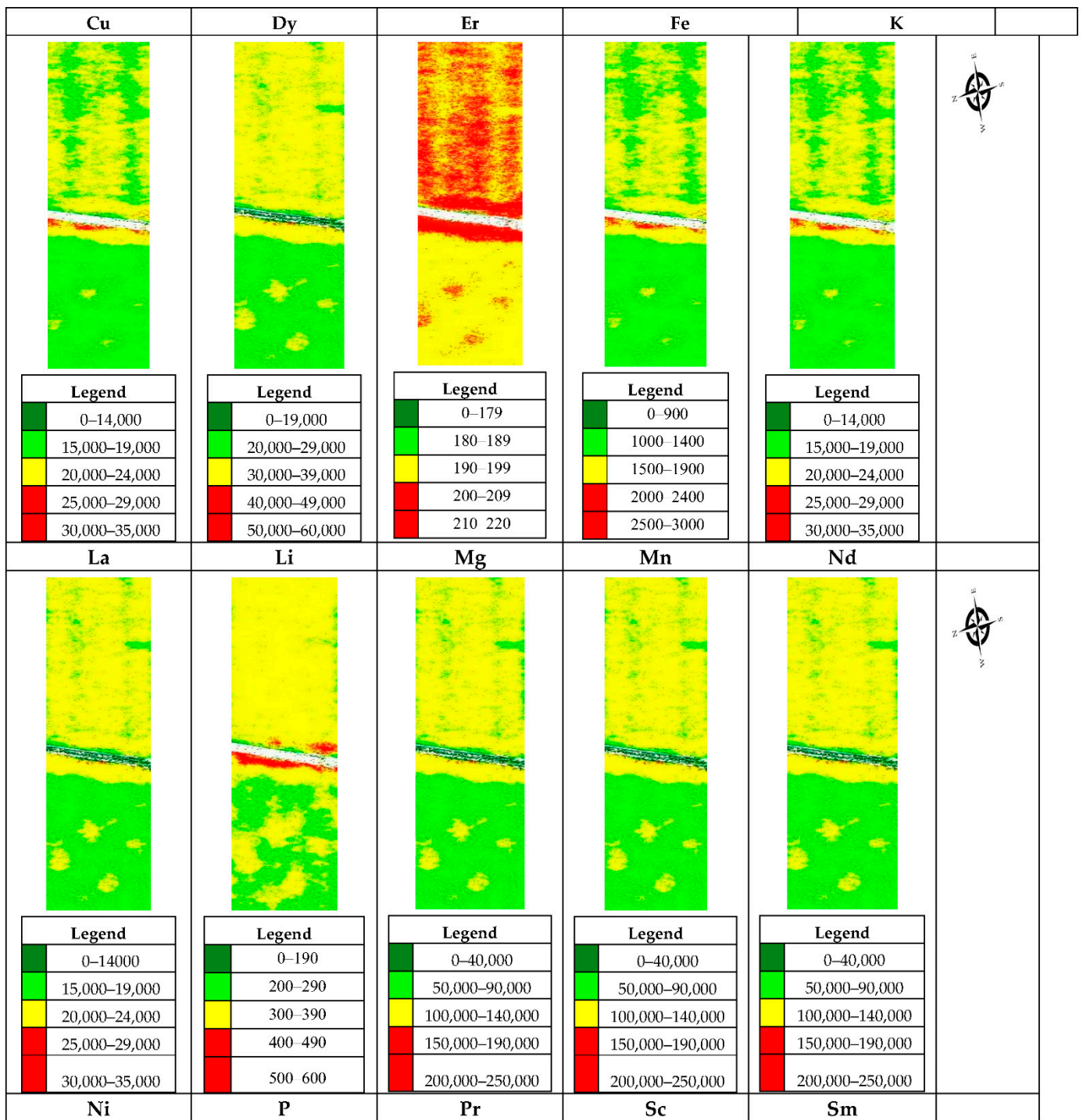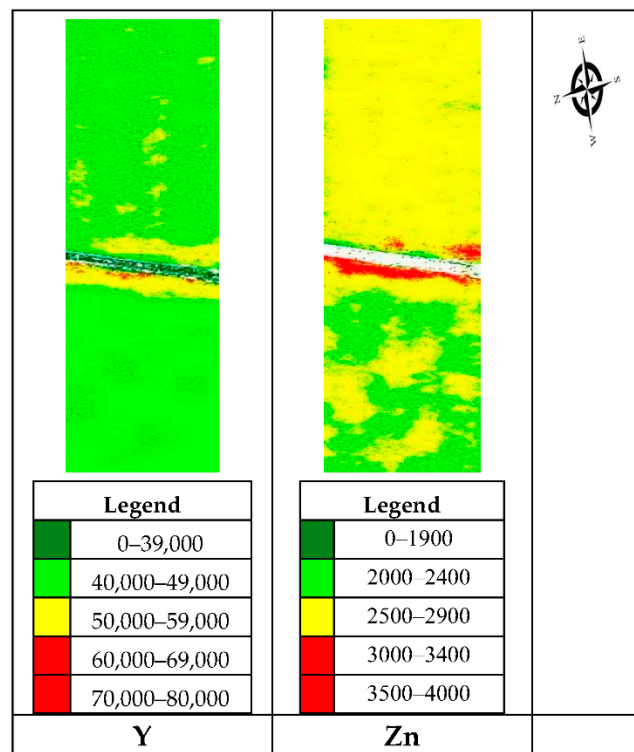| Cu	Dy	Er	Fe	K	
Legend	**Legend**	**Legend**	**Legend**	**Legend**	
0–14,000	0–19,000	0–179	0–900	0–14,000	
15,000–19,000	20,000–29,000	180–189	1000–1400	15,000–19,000	
20,000–24,000	30,000–39,000	190–199	1500–1900	20,000–24,000	
25,000–29,000	40,000–49,000	200–209	2000 2400	25,000–29,000	
30,000–35,000	50,000–60,000	210 220	2500–3000	30,000–35,000	
La	**Li**	**Mg**	**Mn**	**Nd**	
Legend	**Legend**	**Legend**	**Legend**	**Legend**	
0–14000	0–190	0–40,000	0–40,000	0–40,000	
15,000–19,000	200–290	50,000–90,000	50,000–90,000	50,000–90,000	
20,000–24,000	300–390	100,000–140,000	100,000–140,000	100,000–140,000	
25,000–29,000	400–490	150,000–190,000	150,000–190,000	150,000–190,000	
30,000–35,000	500 600	200,000–250,000	200,000–250,000	200,000–250,000	
Ni	**P**	**Pr**	**Sc**	**Sm**	

Figure 4. *Cont.*

Figure 4. Distribution map of levels of (Al, Ca, Ce, Co, Cr, Cu, Dy, Er, Fe, K, La, Li, Mg, Mn, Nd, Ni, P, Pr, Sc, Sm, Y, and Zn) metals in dust.

Table 5. Regression estimates of (Al, Ca, Ce, Co, Cr, Cu, Dy, Er, Fe, K, La, Li, Mg, Mn, Nd, Ni, P, Pr, Sc, Sm, Y, and Zn) metals and UAV parameters.

Metal	Parameter	Coefficients	*p*-Value	Formula
Al/m^2	Red	33.842 **	0.014	0.3029x + 119.14
Ca/m^2	Red	46.509 **	0.052	0.1813x + 119.59
Ce/m^2	Red	0.129 **	0.012	80.567x + 119.08
Co/m^2	Red	0.027 **	0.011	366.22x + 118.86
Cr/m^2	Red	0.063 **	0.013	135.44x + 117.26
Cu/m^2	Red	0.165 **	0.045	52.174x + 118.55
Dy/m^2	Red	0.008 **	0.059	1028x + 121.05
Er/m^2	Red	0.008 *	0.071	980x + 120.07
Fe/m^2	Red	68.578 **	0.017	0.1441x + 118.99
K/m^2	Red	9.009 **	0.044	0.9246x + 119.04
La/m^2	Red	0.063 ***	0.011	162.11x + 119.01
Li/m^2	Red	0.051 ***	0.005	235.22x + 119.67
Mg/m^2	Red	20.183 **	0.024	0.484x + 119.49
Mn/m^2	Red	0.911 **	0.010	11.581x + 119.18
Nd/m^2	Red	0.059 **	0.010	172.79x + 118.92
Ni/m^2	Red	0.050 **	0.032	157.53x + 117.91
P/m^2	Red	5.008 **	0.024	1.7508x + 118.01
Pr/m^2	Red	0.011 **	0.019	933.94x + 119.7
Sc/m^2	Red	0.011 ***	0.019	933.94x + 119.7
Sm/m^2	Red	0.011 ***	0.019	933.94x + 119.7
Y/m^2	Red	0.035 ***	0.005	315.73x + 119.3
Zn/m^2	Red	0.506 **	0.014	18.833x + 118.3
Multiple R	0.942			
R Square	0.888			

***, **, and * indicate 1%, 5%, and 10% levels of significance, respectively.

Table 6. Correlation matrix between (Al, Ba, Fe, K, Na) metals and UAV parameters.

	Blue_av	Cyan	Gray	Green	Hue	Intensity	Magenta	Red	Saturation	Yellow
Al/m^2	0.84	−0.84	0.83	0.84	0.40	0.84	−0.84	0.84	−0.12	−0.84
Ba/m^2	0.85	−0.85	0.84	0.85	0.34	0.85	−0.85	0.85	−0.06	−0.85
Fe/m^2	0.86	−0.86	0.85	0.86	0.36	0.86	−0.86	0.86	−0.05	−0.87
K/m^2	0.64	−0.64	0.63	0.62	0.39	0.65	−0.62	0.64	−0.04	−0.64
Na/m^2	0.85	−0.85	0.85	0.84	0.45	0.86	−0.84	0.85	−0.15	−0.85

The metals Al, Ba, and Fe in snow demonstrated the best regression with the red parameter, with P-values of 0.032 (Al), 0.008 (Ba), and 0.011 (Fe). K and Na metals, on the other hand, displayed a positive relationship with the intensity parameter. Similar to metal characteristics in water, the synergistic effects of the UAV parameters on metals in snow corresponded to the red parameter and were mostly focused on Al, Ba, and Fe metals. Furthermore, the red parameter had a synergistic effect on the absorption of all metals along the road's edge, whereas the intensity parameter exhibited antagonistic effects on the absorption of K and Na metals. This was demonstrated by higher concentrations of Fe, followed by K, Na, Al, and Ba metals on the east side of the road compared to the west side. The obvious distinctive factors in the detection of metals in snow, similar to water, were the level of contamination and the UAV parameters with the most synergistic impact. In the case of this study, the red parameter had the greatest impact.

The presence of dust in the snow demonstrated the high degree of pollution found. Figure 5 displays the visual distribution of metals in snow based on their associated factors. The regression coefficients are shown in Table 7.
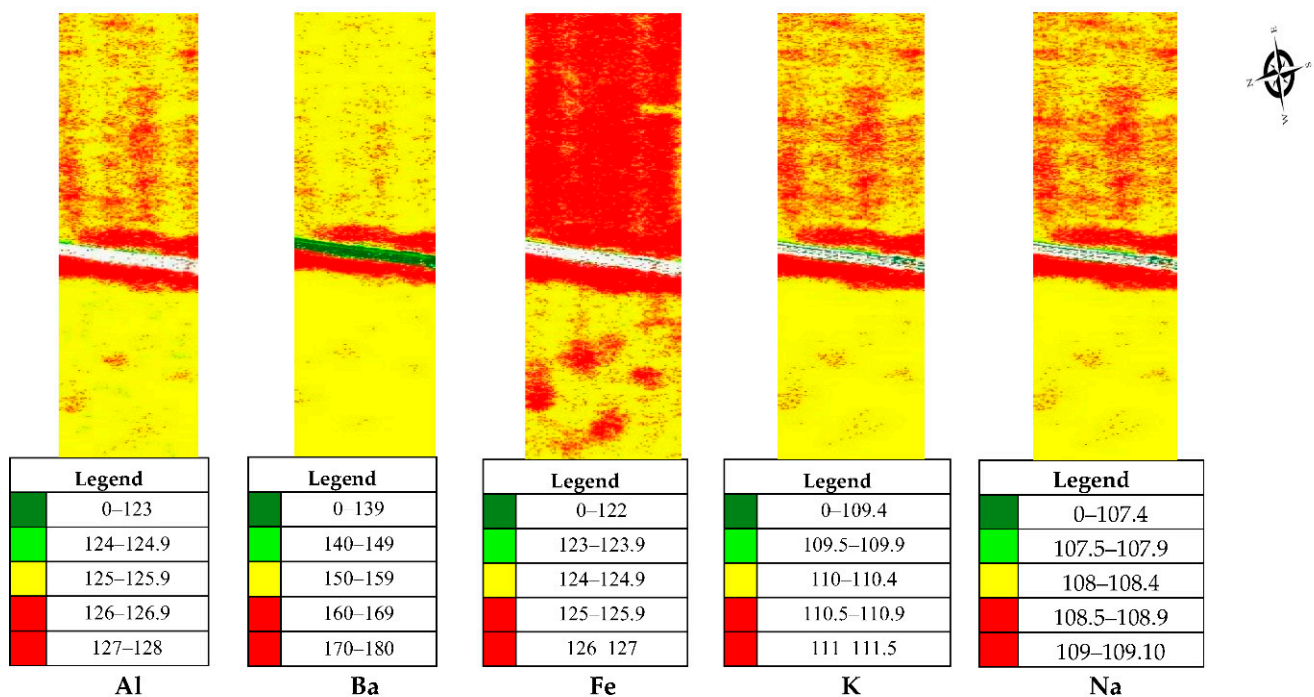

Figure 5. Distribution map of levels of (Al, Ba, Fe, K, and Na) metals in snow.

Table 7. Regression estimates of (Al, Ba, Fe, K, and Na) metals and UAV parameters.

Metal	Parameter	Coefficients	*p*-Value	Formula
Al/m^2	Red	174.530 **	0.032	0.0488x + 117.78
Ba/m^2	Red	48.310 ***	0.008	0.2384x + 118.91
Fe/m^2	Red	229.709 **	0.011	0.046x+ 117.48
K/m^2	Intensity	539.699 ***	0.006	0.017x + 107.92
Na/m^2	Intensity	744.855 *	0.069	0.0082x + 107.12
Multiple R	0.941			
R Square	0.886			

***, **, and * indicate 1%, 5%, and 10% levels of significance, respectively.

4. Discussion

4.1. The Influence of Roadways on Metal Dissemination

Several scientists have demonstrated that the influence zone of dust is approximately 150–180 m from the road [39,40], but the zone was spatially different for various metals in our case. The distribution maps of metals in snow that we acquired typically indicated that the road impact zone was approximately 30 to 90 m, which was less than the impact zones estimated by standard field methods [41]. This was most likely because the width of the impact zone is proportional to the intensity of traffic on a particular highway, as reported by ref. [42]. Another factor could be the distinctly different distribution profiles of coarse particles (2.5 μm < *dp* < 10 μm) and PM$_{2.5}$ (*dp* < 2.5 μm), which was demonstrated by ref. [43].

Our findings that Fe, Zn, Ca, and Al were the most abundant metals in PM$_{2.5}$ while Ca, Fe, Al, and Mg were the most abundant metals in coarse PM were confirmed by the results presented by ref. [43]. The metal distribution patterns in PM$_{2.5}$ and coarse PM were similar, but their magnitudes differed, with Cd, Cr, Cu, Mn, Ni, and Zn claiming a much larger portion in PM$_{2.5}$.

Cd, Cr, Cu, NI, Pb, and Zn are among the most common metal contaminates derived from roadways [44], but we discovered that Al, Fe, K, and Na metals were predominant in water, dust, and snow from the test site. These finding can be attributed to anthropogenic factors such as the use of de-icing agents on roads during the winter, fertilizer applications, and the direction of the area's prevailing wind.

Our experiments discovered that Al, Fe, K, and Na metals had high concentrations and high mobility rates in water, dust, and snow. Despite higher Ca and Mg metal levels, their presence was only detected in dust particles. The metals Ce, Co, Cr, Cu, Dy, Er, La, Li, Mn, Nd, Ni, P, Pr, Sc, Sm, Y, and Zn in dust particles, which were mostly present in residual form, were mostly of natural origin in the studied samples, were not highly mobilized, and were present in low quantities, which aligned with the results presented in ref. [44].

A metal's mobility in water, dust, and snow might be traced to its physical and chemical properties. Based on their studies, the authors of ref. [43,45] affirmed the assertion that transition metals Zn, Cd, and Cu were the most soluble and Cr, Fe, and Ni were the least soluble, highlighting the importance of bioavailability in understanding the impact of transition metals on particle toxicity. Ref. [46] discovered that 63–71% of heavy metals were associated with particles smaller than 250 μm. Additionally, the smaller particle size fraction had a higher metal content, low density, and high mobility in runoff, thus posing a higher risk to the stream network. Ref. [47] reported that most metals in snow exhibited increased concentrations with decreasing pH, which enhanced their mobility. The high levels of Al, Ba, Fe, K, and Na metals in snow may be attributed to the alkalinity of the test site and they were regarded as the most mobile metals in snow.

The resuspension, deposition, and absorption of metals in water, dust, and snow are mainly attributed to road traffic, mostly through the breakdown and resuspension of coarse asphalt particles into fine particles by vehicular movements. Most of these particles end up in the atmosphere and on the edges of roadways.

Our findings showed that the chemical and physical properties of Al, Ba, Fe, K, and Na metals in snow varied depending on environmental factors such as temperature, pressure, polarity, molecular size, and alkalinity, which confirmed the results of ref. [48]. As a result, these factors influenced metal mobility in water, dust, and snow.

4.2. A Remote Sensing Approach for Monitoring Metal Pollution

Remote sensing data can be used as a tool for metal monitoring [49,50]. However, the use of satellite data has serious limitations due to cloud influence and the spatial resolution of remote sensing data.

Several scientists used hyperspectral data for metal mapping and monitoring [51,52]. This technique only offers information at a certain point in the assessment process, making it impossible to establish a detailed image of the dispersion of dusty particulates along highways. Repetitive sampling over time, which is costly and labor-intensive, does not allow for the collection of pollution data at precise sites but over only over a specified region [53], which adds to its challenges. We propose to overcome these limitations using UAVs. We suggested using a simple camera, which was cheaper, but the quality of the results were the same or better when compared with the results of ref. [54,55]. This technique is generic and can detect the levels of various metals and their distribution in the environment, such as roadways. On this foundation, we obtained information for the entire terrain reflecting all of its spatial features, specifically the micro-relief, and snow accumulation irregularities, which may have a significant impact on the distribution of metals in snow. Ref. [56] demonstrated this approach and our results confirmed these findings.

Ref. [57] reported that Cd, Co, Cr, Cu, Fe, Hg, Mn, Mo, Ni, Pb, and Zn metals can be detected based on remote sensing data. We found that only Al, Ba, Fe, K, and Na metals could be detected in snow. This was possible by employing UAV data and establishing the association between the metal content and the pixels of the separated UAV image colors. This technique aligned the metals with their unique corresponding color images (pixels), based on their content and distribution level for detection.

Several studies, including ref. [58], have investigated the spatiotemporal interpolation of UAV data and created a prototype of a standalone interpolation tool that uses radial basis functions (RBF) and inverse distance weighting (IDW) interpolation in a continuous space-time domain. Ref. [59] also demonstrated the successful application of USV to evaluate interpolation methods for distribution maps in chlorophyll-a monitoring. Because the transfer of this model to other regions or plots was not possible in this study, we only used the UAV to interpolate field point measurements. The findings of ref. [60] also affirmed the use of UAV data in spatial interpolation methods for assessing air quality in open-cast mines in an efficient and safe manner.

This study created an effective model for detecting Al, Ba, Fe, K, and Na pollution in snow. Furthermore, we discovered high pollution at 30–190 m from the roadway using UAV data. This model is advantageous for quickly tracking down high-pollution areas. It subsequently allows investigation and mitigation work to be accomplished in less time and at lower cost than conventional methods [61].

5. Conclusions

This paper proposes a technique in which UAV-based data may be utilized to detect metals in dust in snow-covered polluted locations. To support our claim, we evaluated the relationship between various metals in water (melted snow), dust, and snow with various UAV parameters.

The roadway was shown to be a polluter since samples approximately 30 to 50 m from the road had the highest metal concentrations, which declined with distance. In the case of Al, Ca, Fe, K, Na, and Mg metals, the occurrence of high metal distribution east of the highway may be attributed to the predominant wind direction at the test location throughout the research period (Figures 2–4).

Al, Ba, Fe, K, and Na were shown to be visible in snow-covered polluted locations due to dust dispersal. UAV-based data improved the capability of identifying total metals in a mixture of dust and snow. Nonetheless, dust deposits are the best sign of pollution in snow. This discovery supports the claim that UAV indicators may be used to monitor untouchable pollution from roadways.

Author Contributions: Investigation: G.A.B., I.Y.S. and Y.I.V., writing-original draft preparation, G.A.B., I.Y.S. and Y.I.V. All authors have read and agreed to the published version of the manuscript.

Data Availability Statement: The datasets generated and/or analyzed during the study are available from the corresponding author upon request.

Conflicts of Interest: The authors declare no conflict of interest.

Appendix A

For ground control of the UAV, we used 5 points, for which coordinates were obtained based on GNSS (geodesic class equipment, approximately 2 cm error in coordinate assessment). The average error for coordinate assessment by UAV was +/− 10 cm.

Table A1. Heavy metal levels in water from snow samples ($\mu g/m^2$).

Heavy Metal	Distance from the Road (m) and Point Code																		
	190	170	150	130	110	90	70	50	30	0	30	50	70	90	110	130	150	170	190
	9W	8W	7W	6W	5W	4W	3W	2W	1W		1E	2E	3E	4E	5E	6E	7E	8E	9E
Al	5.9	6.2	5.9	6.6	6.2	5.8	99.2	5.3	136		490.3	414.9	89.9	82.6	31.4	164	83.6	116.5	47.4
B	5.928	6.244	5.942	6.608	6.206	5.758	6.842	5.262	6.8		3.922	5.186	5.138	5.16	4.49	4.686	4.52	5.296	4.738
Ba	5.928	6.244	5.942	6.608	6.206	5.758	6.842	5.262	6.8		34.9058	91.2736	5.138	5.16	4.49	4.686	4.52	5.296	4.738
Ca	1482	1267.53	1732.09	1100.23	1337.39	1203.42	1724.18	1360.23	2196.4		2686.57	8245.74	1685.26	1609.92	1012.5	1363.63	935.64	884.432	803.091
Cd	5.928	6.244	5.942	6.608	6.206	5.758	6.842	5.262	6.8		3.922	5.186	5.138	5.16	4.49	4.686	4.52	5.296	4738
Ce	5.928	6.244	5.942	6.608	6.206	5.758	6.842	5.262	6.8		3.922	5.186	5.138	5.16	4.49	4.686	4.52	5.296	4.738
Co	5.928	6.244	5.942	6.608	6.206	5.758	6.842	5.262	6.8		3.922	5.186	5.138	5.16	4.49	4.686	4.52	5.296	4.738
Cr	5.928	6.244	5.942	6.608	6.206	5.758	6.842	5.262	6.8		3.922	5.186	5.138	5.16	4.49	4.686	4.52	5.296	4.738
Cu	5.928	6.244	5.942	6.608	6.206	5.758	6.842	5.262	6.8		3.922	5.186	5.138	5.16	4.49	4.686	4.52	5.296	4.738
Dy	5.928	6.244	5.942	6.608	6.206	5.758	6.842	5.262	6.8		3.922	5.186	5.138	5.16	4.49	4.686	4.52	5.296	4.738
Er	5.928	6.244	5.942	6.608	6.206	5.758	6.842	5.262	6.8		3.922	5.186	5.138	5.16	4.49	4.686	4.52	5.296	4.738
Eu	5.928	6.244	5.942	6.608	6.206	5.758	6.842	5.262	6.8		3.922	5.186	5.138	5.16	4.49	4.686	4.52	5.296	4.738
Fe	59.28	62.44	59.42	66.08	62.06	57.58	68.42	52.62	68		482.406	371.058	51.38	51.6	44.9	46.86	45.2	52.96	47.38
Gd	5.928	6.244	5.942	6.608	6.206	5.758	6.842	5.262	6.8		3.922	5.186	5.138	5.16	4.49	4.686	4.52	5.296	4738
Ho	5.928	6.244	5.942	6.608	6.206	5.758	6.842	5.262	6.8		3.922	5.186	5.138	5.16	4.49	4.686	4.52	5.296	4.738
K	334.932	508.886	843.764	379.96	887.458	702.476	478.94	939.267	503.2		2142.01	710.482	1073.84	665.64	374.915	414.711	316.4	278.04	246.376
La	5.928	6.244	5.942	6.608	6.206	5.758	6.842	5.262	6.8		3.922	5.186	5.138	5.16	4.49	4.686	4.52	5.296	4.738
Li	5.928	6.244	5.942	6.608	6.206	5.758	6.842	5.262	6.8		3.922	5.186	5.138	5.16	4.49	4.686	4.52	5.296	4.738
Lu	5.928	6.244	5.942	6.608	6.206	5.758	6.842	5.262	6.8		3.922	5.186	5.138	5.16	4.49	4.686	4.52	5.296	4.738
Mg	305.292	290.346	317.897	257.712	269.961	299.416	335.258	373.602	499.8		372.59	570.46	418.747	322.5	237.97	304.59	196.62	204.796	161.092

Table A1. *Cont.*

Heavy Metal	Distance from the Road (m) and Point Code																		
	190	170	150	130	110	90	70	50	30	0	30	50	70	90	110	130	150	170	190
	9W	8W	7W	6W	5W	4W	3W	2W	1W		1E	2E	3E	4E	5E	6E	7E	8E	9E
Mn	5.928	6.244	5.942	6.608	6.206	5.758	6.842	5.262	6.8		3.922	5.186	5.138	5.16	4.49	4.686	4.52	5.296	4.738
Na	207.48	437.08	1782.6	726.88	837.81	1727.4	957.88	1841.7	3060		3333.7	2333.7	1798.3	1806	763.3	937.2	723.2	926.8	615.94
Nd	5.928	6.244	5.942	6.608	6.206	5.758	6.842	5.262	6.8		3.922	5.186	5.138	5.16	4.49	4.686	4.52	5.296	4.738
Ni	5.928	6.244	5.942	6.608	6.206	5.758	6.842	5.262	6.8		3.922	5.186	5.138	5.16	4.49	4.686	4.52	5.296	4.738
P	5.928	6.244	5.942	6.608	6.206	5.758	6.842	5.262	6.8		39.22	51.86	51.38	51.6	44.9	46.86	45.2	52.96	47.38
Pb	5.928	6.244	5.942	6.608	6.206	5.758	6.842	5.262	6.8		39.22	51.86	51.38	51.6	44.9	46.86	45.2	52.96	47.38
Pr	5.928	6.244	5.942	6.608	6.206	5.758	6.842	5.262	6.8		3.922	5.186	5.138	5.16	4.49	4.686	4.52	5.296	4.738
Sc	5.928	6.244	5.942	6.608	6.206	5.758	6.842	5.262	6.8		3.922	5.186	5.138	5.16	4.49	4.686	4.52	5.296	4.738
Sm	5.928	6.244	5.942	6.608	6.206	5.758	6.842	5.262	6.8		3.922	5.186	5.138	5.16	4.49	4.686	4.52	5.296	4.738
Sr	5.928	6.244	5.942	6.608	6.206	5.758	6.842	5.262	6.8		3.922	5.186	5.138	5.16	4.49	4.686	4.52	5.296	4.738
Tb	5.928	6.244	5.942	6.608	6.206	5.758	6.842	5.262	6.8		3.922	5.186	5.138	5.16	4.49	4.686	4.52	5.296	4.738
Tm	5.928	6.244	5.942	6.608	6.206	5.758	6.842	5.262	6.8		3.922	5.186	5.138	5.16	4.49	4.686	4.52	5.296	4.738
Y	5.928	6.244	5.942	6.608	6.206	5.758	6.842	5.262	6.8		3.922	5.186	5.138	5.16	4.49	4.686	4.52	5.296	4.738
Yb	5.928	6.244	5.942	6.608	6.206	5.758	6.842	5.262	6.8		3.922	5.186	5.138	5.16	4.49	4.686	4.52	5.296	4.738
Zn	77.064	53.074	30.3042	62.776	93.09	5.758	239.47	36.834	6.8		56.869	33.709	5.138	30.96	29.185	25.3044	94.92	31.776	4.738

Table A2. Heavy metal levels in dust from snow samples (μg/m^2).

Heavy Metal	Distance from the Road (m) and Point Code																		
	190	170	150	130	110	90	70	50	30	0	30	50	70	90	110	130	150	170	190
	9W	8W	7W	6W	5W	4W	3W	2W	1W		1E	2E	3E	4E	5E	6E	7E	8E	9E
Al	0.22	0.15	0.38	0.54	1.06	1.8	2.8	3.67	9.47		108.63	53.24	22.68	18.48	6.76	13.57	1.41	3.37	0.98
B	0	0	0	0	0	0.01	0.01	0.03	0.03		0.09	0.05	0.02	0.03	0.01	0.04	0	0	0
Ba	0.03	0.05	0.11	0.26	0.08	0.15	0.89	3.34	0.84		87.5	6.12	14.37	1.09	2.08	0.75	0.15	0.24	0.1
Ca	1	0.56	1	1	2.59	4.35	6.36	7.63	24.05		187.68	73.26	18.65	22.59	10.48	6.26	1.21	1.9	1.19
Cd	0	0	0	0	0	0	0	0	0		0	0	0	0	0	0	0	0	0
Ce	0	0	0	0	0.01	0.01	0.02	0.02	0.03		0.4	0.22	0.1	0.07	0.02	0.04	0	0.01	0
Co	0	0	0	0	0	0	0	0.01	0.01		0.09	0.05	0.02	0.02	0.01	0.01	0	0	0
Cr	0.01	0	0	0.01	0.01	0.02	0.03	0.04	0.06		0.25	0.15	0.1	0.06	0.03	0.03	0.01	0.01	0
Cu	0	0.01	0.01	0.01	0.02	0.02	0.03	0.08	0.1		0.66	0.25	0.22	0.11	0.06	0.04	0.01	0.01	0.01
Dy	0	0	0	0	0	0	0	0	0		0.03	0.01	0	0	0	0	0	0	0
Er	0	0	0	0	0	0	0	0	0		0.03	0.01	0.01	0.01	0	0	0	0	0
Eu	0	0	0	0	0	0	0	0	0		0	0	0	0	0	0	0	0	0
Fe	0.79	0.5	1.12	2.04	2.82	4.98	7.2	12.54	25.25		232.94	110.26	52.42	43.47	17.68	17.88	2.95	4.89	2.37
Gd	0	0	0	0	0	0	0.01	0.01	0.01		0.04	0.02	0.01	0.01	0	0	0	0	0
Ho	0	0	0	0	0	0	0	0	0		0	0	0	0	0	0	0	0	0
K	0.11	0.1	0.37	0.2	0.39	0.89	1.21	2.18	5.77		37.42	15.22	6.86	6.26	2.06	3.07	0.42	0.72	0.28
La	0	0	0	0	0	0	0.01	0.01	0.02		0.2	0.11	0.05	0.04	0.01	0.02	0	0.01	0
Li	0	0	0	0	0	0	0	0	0		0.13	0.07	0.03	0.02	0.01	0.02	0	0	0
Lu	0	0	0	0	0	0	0	0	0		0.01	0	0	0	0	0	0	0	0
Mg	0.18	0.15	0.25	0.31	0.2	1.2	1.81	2.4	5.1		68.8	30.59	10.79	10.23	4.17	3.55	0.57	1.03	0.48

Table A2. *Cont.*

Heavy Metal	Distance from the Road (m) and Point Code																		
	190	170	150	130	110	90	70	50	30	0	30	50	70	90	110	130	150	170	190
	9W	8W	7W	6W	5W	4W	3W	2W	1W		1E	2E	3E	4E	5E	6E	7E	8E	9E
Mn	0	0	0	0.01	0.01	0.05	0.11	0.08	0.22		2.78	1.54	0.53	0.4	0.16	0.35	0.03	0.09	0.02
Na	0.03	0.05	0.2	0.14	0.13	0.35	0.74	1.96	3.97		22.93	6.04	4.94	1.61	1.19	0.69	0.13	0.17	0.08
Nd	0	0	0	0	0	0.01	0.01	0.01	0.02		0.19	0.1	0.05	0.03	0.01	0.02	0	0.01	0
Ni	0	0	0	0.01	0.01	0.01	0.02	0.04	0.04		0.22	0.11	0.06	0.05	0.02	0.02	0	0.01	0
P	0.26	0.3	0.43	0.42	0.93	1.13	2.31	2.73	3.01		19.61	10.5	4.99	3.94	1.79	1.17	0.32	0.43	0.36
Pb	0.02	0	0	0	0.01	0.04	0.02	0.03	0.03		0.14	0.06	0.05	0.08	0.03	0.02	0	0	0
Pr	0	0	0	0	0	0	0	0	0		0.03	0.01	0.01	0.01	0	0	0	0	0
Sc	0	0	0	0	0	0	0	0	0		0.03	0.01	0.01	0.01	0	0	0	0	0
Sm	0	0	0	0	0	0	0	0	0		0.03	0.01	0.01	0.01	0	0	0	0	0
Sr	0	0	0	0	0	0	0	0.04	0.07		1.45	0.27	0.22	0.04	0.04	0.02	0	0.01	0
Tb	0	0	0	0	0	0.01	0.01	0.02	0		0.02	0	0	0	0	0	0	0	0
Tm	0	0	0	0	0	0	0	0	0		0	0	0	0	0	0	0	0	0
Y	0	0	0	0	0	0	0	0	0.01		0.1	0.06	0.02	0.02	0.01	0.01	0	0	0
Yb	0	0	0	0	0	0	0	0	0		0	0	0	0	0	0	0	0	0
Zn	0.03	0.02	0.03	0.05	0.03	0.07	0.14	0.24	0.024		1.82	0.94	0.4	0.33	0.17	0.13	0.02	0.03	0.02

Table A3. Heavy metal levels in snow samples (dust + water) ($\mu g/m^2$).

Heavy Metal	Distance from the Road (m) and Point Code																		
	190	170	150	130	110	90	70	50	30	0	30	50	70	90	110	130	150	170	190
	9W	8W	7W	6W	5W	4W	3W	2W	1W		1E	2E	3E	4E	5E	6E	7E	8E	9E
Al	6.12	6.35	6.28	7.14	7.26	7.6	102	8.97	145.47		598.93	468.14	112.58	101.08	38.16	177.57	85.01	119.87	48.38
B	5.928	6.244	5.942	6.608	6.206	5.768	6.852	5.292	6.83		4.012	5.236	5.158	5.19	4.5	4.726	4.52	5.296	4.738
Ba	5.958	6.294	6.052	6.868	6.286	5.908	7.732	8.602	7.64		122.406	97.3936	19.508	6.25	6.57	5.436	4.67	5.536	4.838
Ca	1483	1268.09	1733.09	1101.23	1339.98	1207.77	1730.54	1367.86	2220.45		2874.25	8319	1703.91	1632.51	1022.98	1369.89	936.85	886.332	804.281
Cd	5.928	6.244	5.942	6.608	6.206	5.758	6.842	5.262	6.8		3.922	5.186	5.138	5.16	4.49	4.686	4.52	5.296	4738
Ce	5.928	6.244	5.942	6.608	6.216	5.768	6.862	5.282	6.83		4.322	5.406	5.238	5.23	4.51	4.726	4.52	5.306	4.738
Co	5.928	6.244	5.942	6.608	6.206	5.758	6.842	5.272	6.81		4.012	5.236	5.158	5.18	4.5	4.696	4.52	5.296	4.738
Cr	5.938	6.244	5.942	6.618	6.216	5.778	6.872	5.302	6.86		4.172	5.336	5.238	5.22	4.52	4.716	4.53	5.306	4.738
Cu	5.928	6.254	5.952	6.618	6.226	5.778	6.872	5.342	6.9		4.582	5.436	5.358	5.27	4.55	4.726	4.53	5.306	4.748
Dy	5.928	6.244	5.942	6.608	6.206	5.758	6.842	5.262	6.8		3.952	5.196	5.138	5.16	4.49	4.686	4.52	5.296	4.738
Er	5.928	6.244	5.942	6.608	6.206	5.758	6.842	5.262	6.8		3.952	5.196	5.148	5.17	4.49	4.686	4.52	5.296	4.738
Eu	5.928	6.244	5.942	6.608	6.206	5.758	6.842	5.262	6.8		3.922	5.186	5.138	5.16	4.49	4.686	4.52	5.296	4.738
Fe	60.07	62.94	60.54	68.12	64.88	62.56	75.62	65.16	93.25		715.346	481.318	103.8	95.07	62.58	64.74	48.15	57.85	49.75
Gd	5.928	6.244	5.942	6.608	6.206	5.758	6.852	5.272	6.81		3.962	5.206	5.148	5.17	4.49	4.686	4.52	5.296	4738
Ho	5.928	6.244	5.942	6.608	6.206	5.758	6.842	5.262	6.8		3.922	5.186	5.138	5.16	4.49	4.686	4.52	5.296	4.738
K	335.042	508.986	844.134	380.16	887.848	703.366	480.15	941.447	508.97		2179.43	725.702	1080.7	671.9	376.975	417.781	316.82	278.76	246.656
La	5.928	6.244	5.942	6.608	6.206	5.758	6.852	5.272	6.82		4.122	5.296	5.188	5.2	4.5	4.706	4.52	5.306	4.738
Li	5.928	6.244	5.942	6.608	6.206	5.758	6.842	5.262	6.8		4.052	5.256	5.168	5.18	4.5	4.706	4.52	5.296	4.738
Lu	5.928	6.244	5.942	6.608	6.206	5.758	6.842	5.262	6.8		3.932	5.186	5.138	5.16	4.49	4.686	4.52	5.296	4.738
Mg	305.472	290.496	318.147	258.022	270.161	300.616	337.068	376.002	504.9		441.39	601.05	429.537	332.73	242.14	308.14	197.19	205.826	161.572
Mn	5.928	6.244	5.942	6.618	6.216	5.808	6.952	5.342	7.02		6.702	6.726	5.668	5.56	4.65	5.036	4.55	5.386	4.758

Table A3. *Cont.*

Heavy Metal	Distance from the Road (m) and Point Code																		
	190	170	150	130	110	90	70	50	30	0	30	50	70	90	110	130	150	170	190
	9W	8W	7W	6W	5W	4W	3W	2W	1W		1E	2E	3E	4E	5E	6E	7E	8E	9E
Na	207.51	437.13	1782.8	727.02	837.94	1727.75	958.62	1843.66	3063.97		3356.63	2339.74	1803.24	1807.61	764.49	937.89	723.33	926.97	616.02
Nd	5.928	6.244	5.942	6.608	6.206	5.768	6.852	5.272	6.82		4.112	5.286	5.188	5.19	4.5	4.706	4.52	5.306	4.738
Ni	5.928	6.244	5.942	6.618	6.216	5.768	6.862	5.302	6.84		4.142	5.296	5.198	5.21	4.51	4.706	4.52	5.306	4.738
P	6.188	6.544	6.372	7.028	7.136	6.888	9.152	7.992	9.81		58.83	62.36	56.37	55.54	46.69	48.03	45.52	53.39	47.74
Pb	5.948	6.244	5.942	6.608	6.216	5.798	6.862	5.292	6.83		39.36	51.92	51.43	51.68	44.93	46.88	45.2	52.96	47.38
Pr	5.928	6.244	5.942	6.608	6.206	5.758	6.842	5.262	6.8		3.952	5.196	5.148	5.17	4.49	4.686	4.52	5.296	4.738
Sc	5.928	6.244	5.942	6.608	6.206	5.758	6.842	5.262	6.8		3.952	5.196	5.148	5.17	4.49	4.686	4.52	5.296	4.738
Sm	5.928	6.244	5.942	6.608	6.206	5.758	6.842	5.262	6.8		3.952	5.196	5.148	5.17	4.49	4.686	4.52	5.296	4.738
Sr	5.928	6.244	5.942	6.608	6.206	5.758	6.842	5.302	6.87		5.372	5.456	5.358	5.2	4.53	4.706	4.52	5.306	4.738
Tb	5.928	6.244	5.942	6.608	6.206	5.768	6.852	5.282	6.8		3.942	5.186	5.138	5.16	4.49	4.686	4.52	5.296	4.738
Tm	5.928	6.244	5.942	6.608	6.206	5.758	6.842	5.262	6.8		3.922	5.186	5.138	5.16	4.49	4.686	4.52	5.296	4.738
Y	5.928	6.244	5.942	6.608	6.206	5.758	6.842	5.262	6.81		4.022	5.246	5.158	5.18	4.5	4.696	4.52	5.296	4.738
Yb	5.928	6.244	5.942	6.608	6.206	5.758	6.842	5.262	6.8		3.922	5.186	5.138	5.16	4.49	4.686	4.52	5.296	4.738
Zn	77.094	53.094	30.3342	62.826	93.12	5.828	239.61	37.074	6.824		58.689	34.649	5.538	31.29	29.355	25.4344	94.94	31.806	4.758

Table A4. UAV/remote sensing parameters of snow cover.

UAV Parameters	Parameters from the Road (m) and Point Code																		
	190	170	150	130	110	90	70	50	30	0	30	50	70	90	110	130	150	170	190
	9W	8W	7W	6W	5W	4W	3W	2W	1W		1E	2E	3E	4E	5E	6E	7E	8E	9E
Blue_av	128	124	124	123	121	125	125	134	141		154	144	131	128	123	124	124	122	123
Cyan	135	135	136	138	141	137	137	127	119		106	115	128	131	135	135	135	141	139
Gray	123	122	120	119	117	121	121	131	138		150	141	128	125	121	121	121	117	119
Green	123	122	120	119	117	121	122	131	138		150	141	127	124	121	121	121	118	119
Hue	147	139	156	151	146	144	140	142	150		157	152	157	161	145	153	155	141	145
Intensity	116	115	114	113	111	115	115	124	130		142	133	121	118	114	115	114	111	112
Magnet	132	133	135	136	138	134	133	124	117		105	114	128	131	134	134	134	137	136
Red	120	120	119	117	114	118	118	128	136		149	140	127	124	120	120	120	114	116
Saturation	6	3	4	6	6	6	6	5	4		5	4	4	4	3	4	3	6	6
Yellow	127	131	131	132	134	130	130	121	114		101	111	124	127	132	131	131	133	132

References

1. Banerjee, A.D. Heavy metal levels and solid phase speciation in street dusts of Delhi, India. *Environ. Pollut.* **2002**, *123*, 95–105. [CrossRef]
2. Margaryan, V.G.; Yerevan State University; Khachatryan, G.A. The current state of dust content in the atmospheric air of Yerevan. *Ser. Earth Sci.* **2022**, *22*, 21–25. [CrossRef]
3. Skorbiłowicz, M.; Skorbiłowicz, E.; Łapiński, W. Assessment of Metallic Content, Pollution, and Sources of Road Dust in the City of Białystok (Poland). *Aerosol Air Qual. Res.* **2020**, *20*, 2507–2518. [CrossRef]
4. Shinggu, D.Y.; Ogugbuaja, V.O.; Toma, I.; Barminas, J.T. Determination of heavy metals in the street duct in Yola, Nigeria. *Afr. J. Pure Appl. Chem.* **2010**, *4*, 17–21.
5. Al-Khashman, O.A. Determination of metal accumulation in deposited street dusts in Amman, Jordan. *Environ. Geochem. Health* **2007**, *29*, 1–10. [CrossRef]
6. Han, T.-H.; Kim, D.-O.; Lee, Y.; Suh, S.-J.; Jung, H.-C.; Oh, Y.-S.; Nam, J.-D. Gold Nanostructures Formed in Ionic Clusters of Perfluorinated Ionomer. *Macromol. Rapid Commun.* **2006**, *27*, 1483–1488. [CrossRef]
7. Mahowald, N.; Kohfeld, K.; Hansson, M.; Balkanski, Y.; Harrison, S.; Prentice, I.C.; Schulz, M.; Rodhe, H. Dust sources and deposition during the last glacial maximum and current climate: A comparison of model results with paleodata from ice cores and marine sediments. *J. Geophys. Res. Atmos.* **1999**, *104*, 15895–15916. [CrossRef]
8. Fedotov, P.S.; Ermolin, M.S.; Karandashev, V.K.; Ladonin, D.V. Characterization of size, morphology and elemental composition of nano-, submicron, and micron particles of street dust separated using field-flow fractionation in a rotating coiled column. *Talanta* **2014**, *130*, 1–7. [CrossRef] [PubMed]

9. Hjortenkrans, D.; Bergbäck, B.; Häggerud, A. New Metal Emission Patterns in Road Traffic Environments. *Environ. Monit. Assess.* **2006**, *117*, 85–98. [CrossRef] [PubMed]

10. Amato, F.; Querol, X.; Johansson, C.; Nagl, C.; Alastuey, A. A review on the effectiveness of street sweeping, washing and dust suppressants as urban PM control methods. *Sci. Total Environ.* **2010**, *408*, 3070–3084. [CrossRef]

11. Hu, B.; Xue, J.; Zhou, Y.; Shao, S.; Fu, Z.; Li, Y.; Chen, S.; Qi, L.; Shi, Z. Modelling bioaccumulation of heavy metals in soil-crop ecosystems and identifying its controlling factors using machine learning. *Environ. Pollut.* **2020**, *262*, 114308. [CrossRef] [PubMed]

12. Wan, D.; Zhang, N.; Chen, W.; Cai, P.; Zheng, L.; Huang, Q. Organic matter facilitates the binding of Pb to iron oxides in a subtropical contaminated soil. *Environ. Sci. Pollut. Res.* **2018**, *25*, 32130–32139. [CrossRef] [PubMed]

13. Shen, B.; Wang, X.; Zhang, Y.; Zhang, M.; Wang, K.; Xie, P.; Ji, H. The optimum pH and Eh for simultaneously minimizing bioavailable cadmium and arsenic contents in soils under the organic fertilizer application. *Sci. Total Environ.* **2019**, *711*, 135229. [CrossRef] [PubMed]

14. Liu, Y.-M.; Liu, D.-Y.; Zhao, Q.-Y.; Zhang, W.; Chen, X.-X.; Xu, S.-J.; Zou, C.-Q. Zinc fractions in soils and uptake in winter wheat as affected by repeated applications of zinc fertilizer. *Soil Tillage Res.* **2020**, *200*, 104612. [CrossRef]

15. Squadrone, S.; Robetto, S.; Orusa, R.; Griglione, A.; Falsetti, S.; Paola, B.; Abete, M.C. Wildlife hair as bioindicators of metal exposure. *Biol. Trace Element Res.* **2022**, *200*, 5073–5080. [CrossRef]

16. Zhang, P.; Qin, C.; Hong, X.; Kang, G.; Qin, M.; Yang, D.; Pang, B.; Li, Y.; He, J.; Dick, R.P. Risk assessment and source analysis of soil heavy metal pollution from lower reaches of Yellow River irrigation in China. *Sci. Total Environ.* **2018**, *633*, 1136–1147. [CrossRef]

17. Zhao, Z.; Yan, S.; Duan, M.; Fu, J.; Wang, Q.; Liu, Z.; Song, F.; Tang, B.; Li, C.; Qin, G.; et al. Assessing heavy metal pollution and potential ecological risk of tea plantation soils. *Int. J. Agric. Biol. Eng.* **2019**, *12*, 185–191. [CrossRef]

18. Hu, Y.; Cheng, H.; Tao, S. The Challenges and Solutions for Cadmium-contaminated Rice in China: A Critical Review. *Environ. Int.* **2016**, *92–93*, 515–532. [CrossRef]

19. Upadhyay, M.K.; Majumdar, A.; Barla, A.; Bose, S.; Srivastava, S. An assessment of arsenic hazard in groundwater–soil–rice system in two villages of Nadia district, West Bengal, India. *Environ. Geochem. Heal.* **2019**, *41*, 2381–2395. [CrossRef]

20. Sakagami, K.L.; Eamada, R.; Kurobe, T. Heavy metal contents in dust fall and soil of National Park for nature study in Tokyo. *Mitteihingen Dtsch. Bodenkd. Gessellscaft* **1982**, *33*, 59–66.

21. Pan, L.; Ma, J.; Hu, Y.; Su, B.; Fang, G.; Wang, Y.; Wang, Z.; Wang, L.; Xiang, B. Assessments of levels, potential ecological risk, and human health risk of heavy metals in the soils from a typical county in Shanxi Province, China. *Environ. Sci. Pollut. Res.* **2016**, *23*, 19330–19340. [CrossRef]

22. ATSDR (Agency of Toxic Substances and Disease Registry). *Toxicological Profile for Lead, Update. Prepared by Clement International Corporation under Contract Number 205 -88-0608 for ATSDR*; U.S. Public Health Services: Atlanta, GA, USA, 1993.

23. Moiz, M.M.; William, A.S.; Raymond, S.H.Y. Introduction to Mixtures Toxicology and Risk Assessment. In *Principles and Practice of Mixtures Toxicology*; WILEY-VCH Verlag GmbH & Co. KGaA: Weinheim, Germany, 2010; pp. 1–21.

24. Yeganeh, M.; Afyuni, M.; Khoshgoftarmanesh, A.-H.; Soffianian, A.-R.; Schulin, R. Health Risks of Metals in Soil, Water, and Major Food Crops in Hamedan Province, Iran. *Hum. Ecol. Risk Assess. Int. J.* **2012**, *18*, 547–568. [CrossRef]

25. Pan, L.; Wang, Y.; Ma, J.; Hu, Y.; Su, B.; Fang, G.; Wang, L.; Xiang, B. A review of heavy metal pollution levels and health risk assessment of urban soils in Chinese cities. *Environ. Sci. Pollut. Res.* **2017**, *25*, 1055–1069. [CrossRef] [PubMed]

26. Huang, Y.; Chen, Q.; Deng, M.; Japenga, J.; Li, T.; Yang, X.; He, Z. Heavy metal pollution and health risk assessment of agricultural soils in a typical peri-urban area in southeast China. *J. Environ. Manag.* **2018**, *207*, 159–168. [CrossRef]

27. Orusa, T.; Orusa, R.; Viani, A.; Carella, E.; Mondino, E.B. Geomatics and EO Data to Support Wildlife Diseases Assessment at Landscape Level: A Pilot Experience to Map Infectious Keratoconjunctivitis in Chamois and Phenological Trends in Aosta Valley (NW Italy). *Remote. Sens.* **2020**, *12*, 3542. [CrossRef]

28. Hafeez, S.; Wong, M.S.; Abbas, S.; Kwok, C.Y.; Nichol, J.; Lee, K.H.; Tang, D.; Pun, L. Detection and monitoring of marine pollution using remote sensing technologies. In *Monitoring of Marine Pollution*; IntechOpen: Vienna, Austria, 2019.

29. Fiorentin, P.; Bettanini, C.; Lorenzini, E.; Aboudan, A.; Colombatti, G.; Ortolani, S.; Bertolo, A. MINLU: An instrumental suite for monitoring light pollution from drones or airballoons. In Proceedings of the 2018 5th IEEE International Workshop on Metrology for AeroSpace (MetroAeroSpace), Rome, Italy, 20–22 June 2018.

30. Nanni, M.; Demattê, J.; Rodrigues, M.; Santos, G.; Reis, A.; Oliveira, K.; Cezar, E.; Furlanetto, R.; Crusiol, L.; Sun, L. Mapping Particle Size and Soil Organic Matter in Tropical Soil Based on Hyperspectral Imaging and Non-Imaging Sensors. *Remote. Sens.* **2021**, *13*, 1782. [CrossRef]

31. Ben-Dor, E. Quantitative remote sensing of soil properties. In *Advances in Agronomy*; Elsevier: Amsterdam, The Netherlands, 2002; pp. 173–243.

32. Pospelov, P.I.; Moscow Automobile and Road Construction State Technical University (MADI); Tatashev, A.G.; Terentyev, A.V.; Karelina, M.Y.; Yashina, M.V. Bartlett Flows And Mathematical Description Of Motor Traffic Flows. *H&ES Res.* **2021**, *13*, 34–41. [CrossRef]

33. Vasil'Ev, E. International competency requirements for public weather forecasters. *Hydrometeorol. Res. Forecast.* **2021**, *3*, 161–171. [CrossRef]

34. Martin, J.; Schneebeli, M. Impact of the sampling procedure on the specific surface area of snow measurements with the IceCube. *EGUsphere* **2022**, *4*, 1–13. [CrossRef]

35. Rocha, F.; Alves, A.; Homem, V. Exploring the Potential of Sewage Sludge as Agricultural Fertilizer: Determination of Heavy Metals and Nutrients by Microwave-Assisted Digestion Followed by ICP-OES Analysis. *J. Chem. Educ.* **2022**, *99*, 3218–3226. [CrossRef]

36. Cicchino, A.; Nadarajah, S. Entropy stable split forms for the flux reconstruction high-order method: Three-dimensional numerical validation. In *Aiaa Aviation 2021 Forum*; American Institute of Aeronautics and Astronautics: Reston, VA, USA, 2021.

37. Treller, A. Explicit Microsoft Excel Methods For Computerized System Validation. *J. Valid. Technol.* **2021**, *27*, 2–4. [CrossRef]

38. Vallidevi, K.; Gopinath, K.P.; Nagarajan, K.K.; Prakash, D.G.; Sudhamsu, G.; Sudhish, S.; Al-Zahrani, S.A. Water Pollution Monitoring through Remote Sensing. *Curr. Anal. Chem.* **2021**, *17*, 802–814. [CrossRef]

39. Phillips, B.B.; Bullock, J.M.; Osborne, J.L.; Gaston, K.J. Spatial extent of road pollution: A national analysis. *Sci. Total Environ.* **2021**, *773*, 145589. [CrossRef] [PubMed]

40. Liu, Y.; Jin, T.; Yu, S.; Chu, H. Pollution characteristics and health risks of heavy metals in road dust in Ma'anshan, China. *Environ. Sci. Pollut. Res.* **2023**, 1–14. [CrossRef] [PubMed]

41. Ahmed, R.S.; Abuarab, M.E.; Ibrahim, M.M.; Baioumy, M.; Mokhtar, A. Assessment of environmental and toxicity impacts and potential health hazards of heavy metals pollution of agricultural drainage adjacent to industrial zones in Egypt. *Chemosphere* **2023**, *318*, 137872. [CrossRef]

42. Zariņš, A.; Smirnovs, J.; Lācis, R. Evaluation Of Air Pollution Measurements In Urban Environment Considering Traffic Intensity. *Constr. Sci.* **2014**, *15*, 29. [CrossRef]

43. Ragimov, A.; Mazirov, M.; Shenterova, E.; Zunimaymayti, A. Features of accumulation of heavy metals in the soil cover of the road territory on the example of the sudogodskiy district of the vladimir region. *Succeses Mod. Nat. Sci. (Adv. Curr. Nat. Sci.)* **2019**, 122–127. [CrossRef]

44. Jiang, S.Y.; Yang, F.; Chan, K.L.; Ning, Z. Water solubility of metals in coarse PM and PM 2.5 in typical urban environment in Hong Kong. *Atmos. Pollut. Res.* **2014**, *5*, 236–244. [CrossRef]

45. Pagotto, C.; Rémy, N.; Legret, M.; Le Cloirec, P. Heavy Metal Pollution of Road Dust and Roadside Soil near a Major Rural Highway. *Environ. Technol.* **2001**, *22*, 307–319. [CrossRef]

46. Chuan, M.C.; Shu, G.Y.; Liu, J.C. Solubility of heavy metals in a contaminated soil: Effects of redox potential and pH. *Water Air Soil Pollut.* **1996**, *90*, 543–556. [CrossRef]

47. Król, A.; Mizerna, K.; Bożym, M. An assessment of pH-dependent release and mobility of heavy metals from metallurgical slag. *J. Hazard. Mater.* **2020**, *384*, 121502. [CrossRef] [PubMed]

48. Zhao, H.; Yin, C.; Chen, M.; Wang, W. Risk Assessment of Heavy Metals in Street Dust Particles to a Stream Network. *Soil Sediment Contam. Int. J.* **2009**, *18*, 173–183. [CrossRef]

49. Rieuwerts, J.; Thornton, I.; Farago, M.; Ashmore, M. Factors influencing metal bioavailability in soils: Preliminary investigations for the development of a critical loads approach for metals. *Chem. Speciat. Bioavailab.* **1998**, *10*, 61–75. [CrossRef]

50. Peng, Y.; Kheir, R.B.; Adhikari, K.; Malinowski, R.; Greve, M.B.; Knadel, M.; Greve, M.H. Digital Mapping of Toxic Metals in Qatari Soils Using Remote Sensing and Ancillary Data. *Remote. Sens.* **2016**, *8*, 1003. [CrossRef]

51. Mouazen, A.M.; Nyarko, F.; Qaswar, M.; Tóth, G.; Gobin, A.; Moshou, D. Spatiotemporal Prediction and Mapping of Heavy Metals at Regional Scale Using Regression Methods and Landsat 7. *Remote. Sens.* **2021**, *13*, 4615. [CrossRef]

52. Xu, Y.; Wang, X.; Cui, G.; Li, K.; Liu, Y.; Li, B.; Yao, Z. Source apportionment and ecological and health risk mapping of soil heavy metals based on PMF, SOM, and GIS methods in Hulan River Watershed, Northeastern China. *Environ. Monit. Assess.* **2022**, *194*, 181. [CrossRef]

53. Neumann, N.N.; Derksen, C.; Smith, C.; Goodison, B. Characterizing local scale snow cover using point measurements during the winter season. *Atmos.-Ocean* **2006**, *44*, 257–269. [CrossRef]

54. Yang, Y.; Christakos, G. Uncertainty assessment of heavy metal soil contamination mapping using spatiotemporal sequential indicator simulation with multi-temporal sampling points. *Environ. Monit. Assess.* **2015**, *187*, 571. [CrossRef]

55. Guo, Y.; Liang, Y.; Deng, R.; Li, J.; Wang, J.; Hua, Z.; Tang, Y. Development and application of a new sensitivity analysis model for the remote sensing retrieval of heavy metals in water. *Heliyon* **2022**, *8*, e12033. [CrossRef]

56. Koziol, K.; Uszczyk, A.; Pawlak, F.; Frankowski, M.; Polkowska, Ż. Seasonal and Spatial Differences in Metal and Metalloid Concentrations in the Snow Cover of Hansbreen, Svalbard. *Front. Earth Sci.* **2021**, *8*, 538762. [CrossRef]

57. Kemper, T.; Sommer, S. Use of airborne hyperspectral data to estimate residual heavy metal contamination and acidification potential in the Guadiamar floodplain Andalusia, Spain after the Aznacollar mining accident. In *Remote Sensing for Environmental Monitoring, GIS Applications, and Geology IV*; Ehlers, M., Posa, F., Kaufmann, H.J., Michel, U., De Carolis, G., Eds.; SPIE: Bellingham, WA, USA, 2004.

58. Strelnikova, D.; Anders, K.-H. Spatio-Temporal Interpolation of UAV Sensor Data. *GI_Forum* **2017**, *1*, 141–156. [CrossRef]

59. Kim, E.; Nam, S.-H.; Ahn, C.H.; Lee, S.; Koo, J.-W.; Hwang, T.-M. Comparison of spatial interpolation methods for distribution map an unmanned surface vehicle data for chlorophyll-a monitoring in the stream. *Environ. Technol. Innov.* **2022**, *28*, 102637. [CrossRef]

60. Nguyen, Q.L.; Cuong, C.X.; VAN Canh, L.; Bich, N.N.; Tran, D.A.; Bui, X.-N. 3D Spatial Interpolation Methods for Open-Pit Mining Air Quality with Data Acquired by Small UAV Based Monitoring System. *Inżynieria Miner.* **2020**, *1*, 263–272. [CrossRef]
61. Chen, H.W.; Chen, C.-Y.; Nguyen, K.L.P.; Chen, B.-J.; Tsai, C.-H. Hyperspectral sensing of heavy metals in soil by integrating AI and UAV technology. *Environ. Monit. Assess.* **2022**, *194*, 518. [CrossRef] [PubMed]